

DOI: 10.61558/2993-074X.3482

Article ID: 1006-3471(2024)00-0000-00

[Http://electrochem.xmu.edu.cn](http://electrochem.xmu.edu.cn)[Https://jelectrochem.xmu.edu.cn/](https://jelectrochem.xmu.edu.cn/)

Highly Sensitive Detection of Strontium Ions Using Metal-Organic Frameworks Functionalized Solid-State Nanochannels

Xu-Gang Wang^a, Zheng-Xu He^a, De-Fang Ding^a, Xue-Qin Luo^a, Li Dai^a, Wei-Qi Zhang^a, Qun Ma^b, Yu Huang^{*a}, Fan Xia^{a,c}

^a State Key Laboratory of Biogeology and Environmental Geology, Engineering Research Center of Nano-Geomaterials of Ministry of Education, Faculty of Material Science and Chemistry, China University of Geosciences, Wuhan 430074, P. R. China

^b Department of Chemical Engineering, Graduate School of Engineering, Osaka Metropolitan University, Sakai, Osaka 599-8570, Japan

^c Shenzhen Research Institute of China University of Geosciences

* Corresponding author: Yu Huang

E-mail: yuhuang@cug.edu.cn

Abstract

Strontium-90, a highly radioactive isotope, accumulates within the food chain and skeletal structure, posing significant risks to human health. There is a critical need for a sensitive detection strategy for Strontium-90 in complex environmental samples. Here, solid-state nanochannels, modified with metal-organic frameworks (MOF) and specific aptamers, were engineered for highly sensitive Sr^{2+} detection. The synergistic effect between the reduced effective diameter of the nanochannels due to MOF and the specific binding of Sr^{2+} by aptamers amplifies the difference in ionic current signals, enhancing detection sensitivity significantly. The MOF-modified nanochannels exhibit highly sensitive detection of Sr^{2+} , with a detection limit (LOD) of 0.03 nM, whereas the LOD for AAOs without the modified MOF nanosheets is only 1000 nM. These findings indicate that the LOD of Sr^{2+} detected by MOF-modified nanochannels is approximately 33,000 times higher than that of the nanochannels without MOF modification. Additionally, highly reliable detection of Sr^{2+} in various water samples was achieved, with a recovery rate ranging from 94.00% to 118.70%. This study provides valuable insights into the rapidly advancing field of advanced nanochannel-based sensors and their diverse applications for analyzing complex samples, including environmental contaminant detection, food analysis, medical diagnostics, and more.

Keywords: Nanochannels; MOF; Sensor; Sr^{2+} ; Sensitivity Detection

1. Introduction

The ocean stands as Earth's most vital natural resources crucial for human survival. Ocean monitoring serves as a crucial method for real-time observation and data collection in marine environments, playing a fundamental role in safeguarding marine ecosystems and ensuring human sustenance and progress [1,2]. Especially, due to the recent Fukushima nuclear wastewater discharge

incident in Japan, marine life is facing numerous uncertainties. Hence, the monitoring of the marine environment, particularly the surveillance of radioactive elements in seawater, has garnered escalating significance in scientific research [3,4].

Traditionally, offshore marine water quality monitoring relies on manual sampling, involving the collection of samples by vessels at specific locations, followed by analysis and processing in onshore laboratories [5]. Current water quality monitoring technologies in laboratories mainly rely on

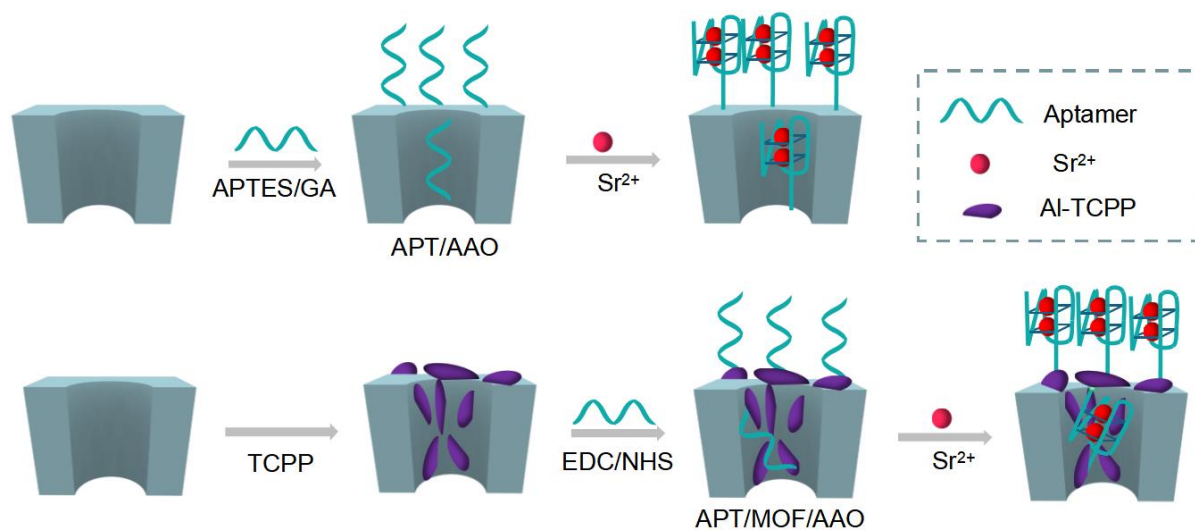
physicochemical monitoring methods such as atomic absorption spectrophotometry [6], ion-selective electrode method [7,8], ion chromatography [9], gas chromatography [10], and inductively coupled plasma atomic emission spectroscopy (ICP-AES) [11]. Utilizing traditional manual sampling and laboratory detection technologies enables the accurate acquisition of samples, flexibility in selecting sampling locations, and a thorough assessment of water quality. However, this method is susceptible to weather and sea conditions and exhibits low efficiency, particularly when monitoring radioactive elements like Strontium-90. The challenge lies in the large sample requirements to detect trace amounts of these elements in seawater, necessitating complex enrichment processes before analysis. Furthermore, current analytical methods entail intricate instrument operation, cumbersome sample handling procedures, slow response times, and limited timeliness. Consequently, there is an urgent call for the development of a portable sensor capable of rapid enrichment, simplified processing, and highly sensitive of radioactive elements in the ocean.

In recent decades, solid-state nanochannels have emerged as chemically and mechanically stable platforms [12-14], offering adjustable dimensions and exceptional enrichment capacity. These attributes address the limitations of traditional methods for trace element enrichment. Moreover, the confined space within nanochannels, coupled with their functionalization strategies, presents a distinct advantage for detection [15-17]. The integration of aptamers into nanochannel sensors through chemical modifications on the nanochannel surface has demonstrated remarkable sensitivity and specificity in target detection. [18-22] Notably, commercial anodized aluminum oxide (AAO) featuring an arrayed nanochannel structure within the 30-200 nm range is extensively employed in constructing solid-state nanochannel-based sensing platforms [23]. For example, Kuang's research group first modified the penicillamine molecule on copper selenide nanoparticles, and then self-assembled the nanoparticles onto AAO to form heterogeneous nanochannels to construct a sensing system. The

detection of limit (LOD) as low as 0.027 nM were achieved [24]. Zeng et al. devised a sensing system employing AAO and mesoporous silica for dopamine detection, achieving a LOD of 0.1 nM [25]. Our research group used AAO to achieve ultra-high sensitivity and specificity for the detection of proteins [26]. On the other hand, leveraging the advantages of Metal-Organic Frameworks (MOF), such as high porosity, large specific surface area, and adjustable structure, MOF-modified nanochannels are regarded as advanced chemical sensors [27-31]. Therefore, with the organic ligand TCPP utilizing aluminum ions provided by AAO to synthesize two-dimensional nanosheets Al-TCPP (MOF) in situ, modifying the inner and outer surfaces of AAO nanochannels, we chose this material to investigate the sensing performance toward Sr^{2+} . However, the direct use of MOF-modified nanochannels for detecting radioactive elements in complex water samples is not yet widespread, and their specific sensing properties in this context remain to be fully elucidated.

Here, a highly sensitive method for detecting Sr^{2+} in complex water was developed by synthesizing binary MOF nanosheets directly on AAO substrate. This method involves modifying a DNA strand capable of folding into G-quadruplexes in response to Sr^{2+} , serving as specific probes (referred to as APT) on the surface of MOF-modified AAOs (APT/MOF/AAO). During the recognition process of Sr^{2+} , the effective pore size of the nanochannels was significantly reduced due to the synergistic effect of specific aptamers and uniformly dispersed 2D nanosheets on both the inner and outer surfaces of the AAO. This resulted in a considerable amplification of the variance in the ionic current signal, showcasing ultra-high sensitivity. Consequently, compared to the APT/AAO detection system, the APT/MOF/AAO detection system significantly improved the LOD from 1000 nM to an ultra-low 0.03 nM, which is lower than the Sr^{2+} concentration in natural seawater (90.1 μM), and the Sr^{2+} concentration in nuclear wastewater (0.1 μM to 1 mM) [32]. Additionally, the general ionic conductivity model of cylindrical nanochannels was employed to elucidate the sensing mechanism of the nanochannels. COMSOL was also utilized to simulate the increase in

ion currents before and after the binding of 7
nanochannels to the target, yielding calculated results 8
that align with the experimental findings. Furthermore, 9
APT/MOF/AAO demonstrated the ability to accurately 10
detect Sr^{2+} nanomolar levels in complex samples such 11
as tap water and mineral water. This research offers



Scheme 1. Schematic diagram of the principle for the aptasensor. It describes the construction of two sensing systems, APT/AAO and APT/MOF/AAO, as well as the process of target identification.

2. Experimental Section

2.1 Chemicals and materials

AAO membranes, with height of 60 μm and the pore size of 80~100 nm, were purchased from Pu Yuan Nano (Hefei, China). Tetras-(4-carboxyphenyl)porphyrin (TCPP), N,N-dimethylformamide (DMF, 99%), isopropanol, and glutaraldehyde 25% aqueous solution were purchased from Sinopharm (Beijing, China). 1-Ethyl-3-(3-dimethylaminopropyl)carbodiimide (EDC), N-hydroxysulfosuccinimide sodium salt (NHS), 3-aminopropyltriethoxysilane (APTES), strontium chloride, Tris-HCl buffer, PBS buffer were purchased from Aladdin (Shanghai, China). Single-stranded Aptamers (5'-NH₂-C₆-AGGGTTAGGGTTAGGGTTAGGGC-3') for Sr^{2+} sensing was purchased from Sangon Biotech Inc. (Shanghai, China). All solutions were made with deionized water (18.2 M Ω cm, Milli-Q system).

2.2 Preparation of APT/AAO

Firstly, AAO was placed in ultrapure water to sonicate for 5 min to remove surface impurities and dried at 60°C for 5 min. Then, the dried AAO is immersed in a pre-prepared 15% APTES isopropanol solution to seal the shading reaction for 12 h. After the reaction was completed, it was washed three times with isopropanol to remove any unreacted APTES. Subsequently, the sample was dried in a 120°C oven for 2 h to obtain APTES-modified AAO. Subsequently, 5% glutaraldehyde aqueous solution was added, which was also sealed for 12 h, and then repeatedly rinsed with deionized water three times to remove the unreacted glutaraldehyde to obtain aldehyde-modified AAO. Finally, the aldehyde-modified AAO was placed in Tris-HCl buffer containing 1 μM Sr^{2+} specific aptamer for 12 h to obtain the aptamer-modified AAO, called APT/AAO.

2.3 Preparation of MOF

To fabricate nanochannel films with smaller and denser pore sizes, certain adjustments were implemented in the experiments, drawing from insights provided in

previous literature. The specific experimental procedure was as follows: TCPP (40 mg) was added to a PTFE liner filled with 25 mL of DMF and ultrapure water mixture ($V_{\text{DMF}}:V_{\text{water}} = 3:1$), mixed evenly, and then sonicated at room temperature for 15 min. Then, the bare AAO membrane after sonication was placed on a PTFE scaffold and immersed in the mixture, then the inner tank was put into the reaction kettle, and sealed and placed in an oven at 120°C for 2 h to obtain MOF modified AAO, which was named MOF. After the reaction was completed, the obtained MOF membranes were washed with DMF and deionized water, respectively, and dried at room temperature in an oven.

2.4 Preparation of ATP/MOF/AAO

To obtain an aptamer-modified MOF membrane (APT/MOF/AAO), the MOF membrane was immersed in PBS buffer (pH = 7.4) containing 1-ethyl-3-(3-dimethylaminopropyl) carbodiimide (50 mg·mL⁻¹) and N-hydroxysulfosuccinimide (25 mg·mL⁻¹) for 1 h to activate the carboxyl groups on the film's surface. Subsequently, the membrane was rinsed three times with deionized water before being immersed in Tris buffer containing the aptamers (10 mM Tris, pH = 7.4) for 12 h^[33] to obtain APT/MOF/AAO. Any unbound aptamers were then removed using deionized water.

2.5 Characterizations of Materials

The surface and cross-sectional morphology of AAO and MOF were characterized by using scanning transmission electron microscopy (FESEM, SU8010, Hitachi). X-ray photoelectron spectroscopy (XPS) was used to characterize AAO, MOF, and APT/MOF/AAO. The morphological characteristics of MOF grown on AAO was characterized by using Atomic Force Microscopy (AFM).

2.6 Current-voltage (I-V) testing methods

According to previous reports, the transmembrane current of the sample was measured in a customized dual electrode system transmembrane current testing device, which includes a pair of separated electrolytic cells, a pair of self-made Ag/AgCl electrodes, electrolyte, and an external picoampere meter (Keithley 6487, Jishili Instruments, USA). The electrolyte used in this work is 10 mM Tris HCl (pH=7.4). The nanochannels membrane to be tested was sandwiched between two electrolyzers and an electric field was applied as a scanning voltage ranging from -1 V to 1 V. Its current-voltage value was recorded by Keithley 6487 picoampere meter. All tests were conducted at room temperature, with at least 5 films measured for each sample to obtain the average current-voltage value.

3. Results and discussion

3.1 Characterization of the *in-situ* growth of TCPP in AAO

FESEM and AFM were employed for the characterization of the surface of both AAO and MOF to confirm the *in-situ* growth of TCPP in AAO. As shown in **Figure 1a** and **b**, presenting the top view and side view of the AAO, respectively, the AAO exhibited a structured array with nanochannels. The pore size of AAO was measured at 88.62 ± 10.60 nm (**Figure S1**). Meanwhile, SEM images displayed the top view and side view of the MOF, respectively (**Figure 1c** and **1d**). SEM images revealed that the outer surface of the AAO was densely covered by 2D nanosheets (**Figure 1c**), and the channels were filled with dense 2D nanosheets (**Figure 1d**) following the *in-situ* growth of TCPP on AAO. Combining **Figure S4**, these results indicate that Al-TCPP has grown on both the inner and outer surfaces of the AAO pore.

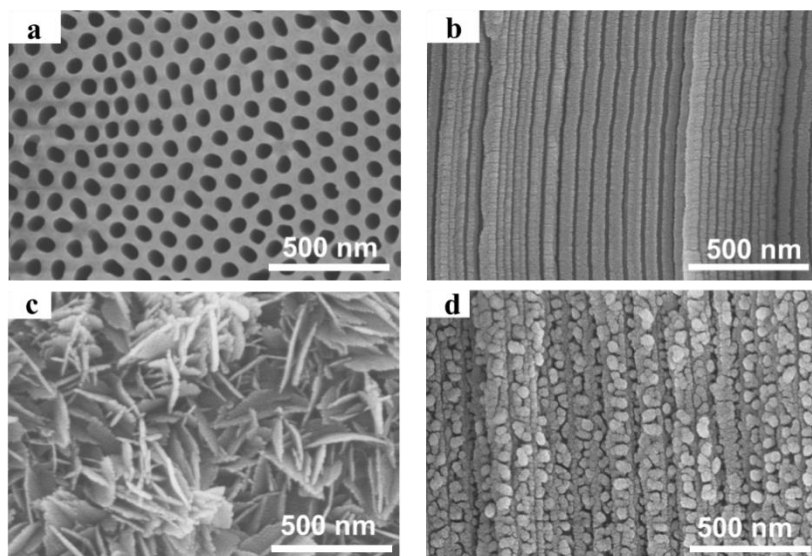


Figure 1. SEM images of AAO and MOF. (a, b) Top and side views of AAO, respectively. (c, d) Top and side views of MOF, respectively. The images demonstrate the successful in-situ growth of the ligand TCPP on AAO, forming MOF modified nanochannels and effectively reducing the diameter of the AAO.

AFM was also utilized to characterize the outer surface of the nanosheets in the outer surface of AAO. From **Figure 2c** and **2d**, the diameter of the nanochannels with successfully modified MOF nanosheets was analyzed using the method outlined in **Figure S2**, yielding an average diameter of approximately 12.1 ± 2.3 nm. These results suggest that the modified MOF nanosheets effectively reduce the channel size of AAO.

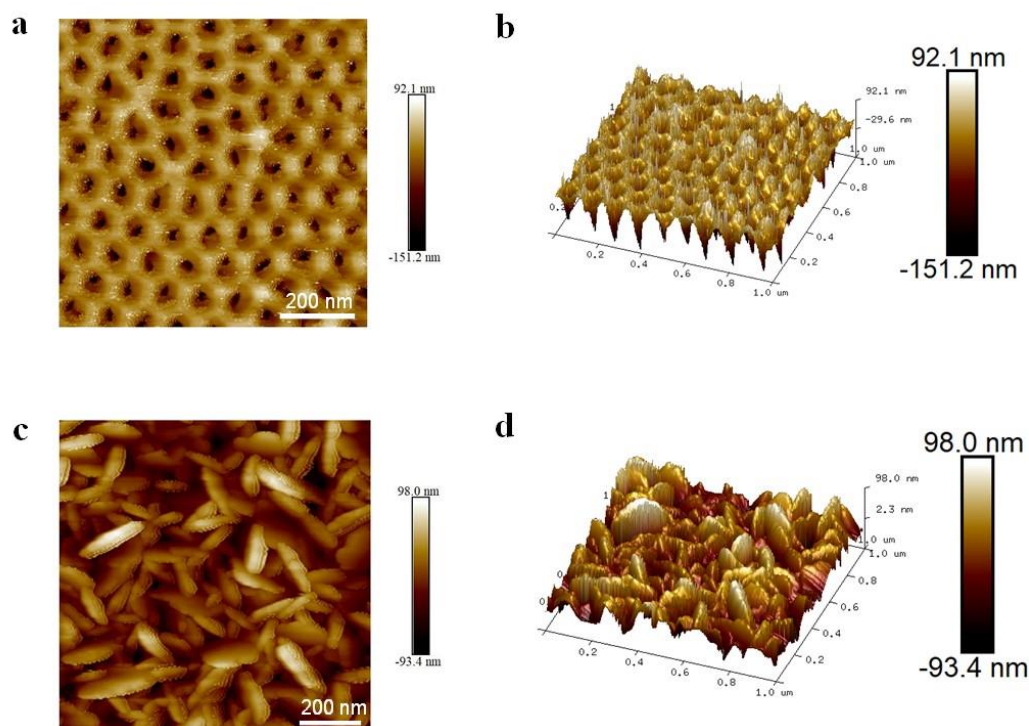


Figure 2. AFM images and pore size analysis of nanochannels. (a, b) 2D and 3D AFM images of AAO, respectively. (c, d) 2D and 3D AFM images of MOF, respectively. The results further confirm the MOF nanosheets were successfully

grown on the outer surfaces of AAO.

3.2 Surface properties of aptamer-modified nanochannels

In this work, the ligand TCPP utilized the metallic aluminum present in AAO to serve as the required metal ions for coupling, enabling the growth of dense MOF two-dimensional nanosheets in situ. Aptamers were employed to modify the AAO and MOF nanochannels by conjugating their amino groups with the carboxyl groups on the nanochannels, which were treated with carboxyl activators. Here, Guanine tetraplexes (G-quadruplexes) were selected as specific sensing probes. Guanine tetraplexes are higher-order structures derived from biological sources formed by folding DNA or ribonucleotides rich in tandem guanine repeats [34]. These structures can be created by stacking two or more G-quadruplexes [35-38]. Studies have shown that in the presence of Sr^{2+} , the linear DNA can fold into a stable G-quadruplex structure [39,40]. The sensors employed in this study were the resulting APT/AAO and APT/MOF/AAO. To confirm the successful grafting of aptamers onto nanochannels, we carefully analyzed the elemental composition of AAO, MOF, and APT/MOF/AAO film surfaces using XPS. As shown in **Figure 3a**, MOF exhibited N elements compared to AAO, resulting in the presence of an N1s peak. The O1s (532.02 eV) peak exhibited significant enhancement after the successful grafting of aptamers onto the MOF, indicating an increase in the content of O elements (**Figure 3b and 3c**). As shown in **Figure 3d**, a distinctive peak of P2p emerged around 133.86 eV, signifying the presence of phosphorus elements from the aptamers on the surface of MOF. Similarly, the N1s (400.98 eV) peak showed a significant enhancement after the aptamer was successfully grafted onto MOF, indicating an increase in the content of N elements (**Figure 3e and 3f**). The heightened intensity of the C-NH₂ and C=O peaks from the bases in the aptamer suggested the successful attachment of aptamers onto the MOF. These XPS findings validate the successful attachment of aptamers onto MOF.

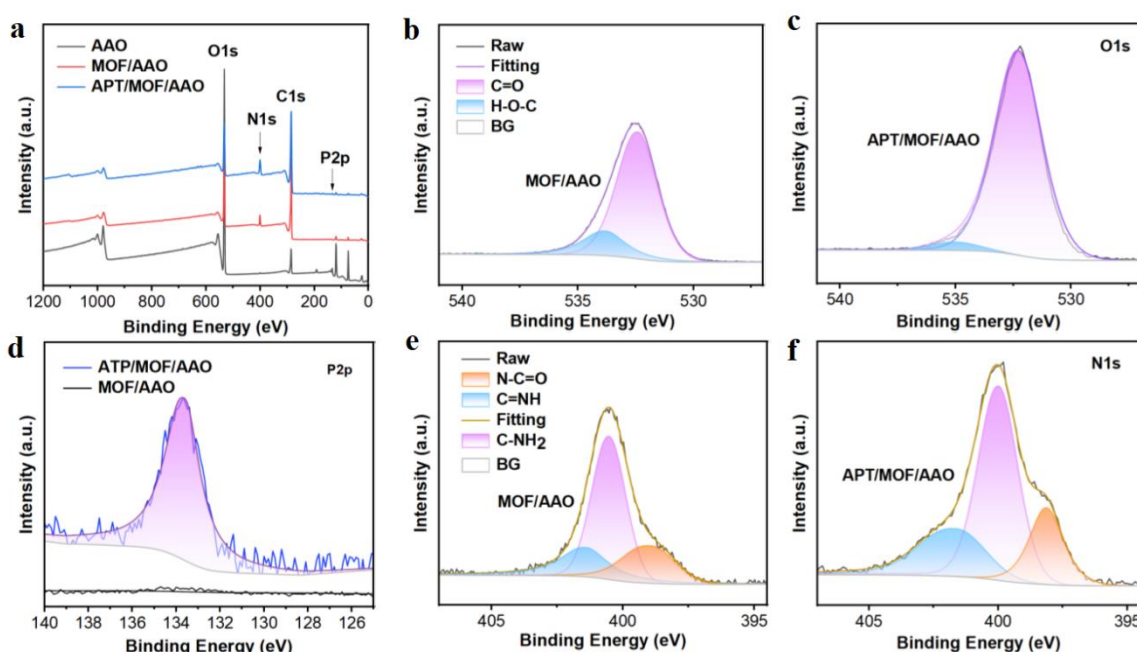


Figure 3. XPS spectra of AAO, MOF, and APT/MOF/AAO. (a) XPS total spectra of bare AAO, MOF and APT/MOF/AAO. (b, c) The narrow spectra of XPS near the O1s peak of MOF and APT/MOF/AAO. (d) The narrow spectra of XPS near the P2p peak of MOF and APT/MOF/AAO. (e, f) The narrow spectra of XPS near the N1s peak of MOF and APT/MOF/AAO. The above results showed that the aptamers were successfully grafted onto MOF to form APT/MOF/AAO.

3.3 Sr²⁺ detection performance of ATP/AAO and APT/MOF/AAO

To illustrate the enhanced sensitivity of APT/MOF/AAO nanochannels in detection, we tested the I-V curves of the APT/AAO and APT/MOF/AAO in response to varying concentrations of Sr²⁺. Upon binding to the target, the initially "stretched" aptamer undergoes a conformational change to form a G-quadruplex structure in response to Sr²⁺ induction. This alteration increases the effective pore size of the nanochannels and subsequently modifies the ion current passing. As shown in **Figure 4a**, transmembrane ion currents were recorded before and after immersion in a 100 nM Sr²⁺ solution using APT/MOF/AAO. Following immersion in the ionic

APT/MOF/AAO increased from 3.99 μ A to 5.80 μ A at 1 V, marking an approximate 45% increase in ion current. The increase of current was mainly due to the formation of G-quadruplex induced by Sr²⁺, triggering a conformational shift in the aptamer within the nanochannels, thereby enlarging the effective channel size and subsequently boosting the current. In the experiment, we defined the transmembrane ion current amplification of the nanochannels as $(I_2 - I_1)/I_1 \times 100\%$, where I_1 and I_2 represented the currents before and after detecting the same concentration of the target at 1 V, respectively. In this work, a 10% rise in transmembrane ion current within the nanochannels was deemed a reliable sensing event. Conversely, increases below 10% were considered ineffective, likely due to factors such as physical adsorption or non-specific interactions.

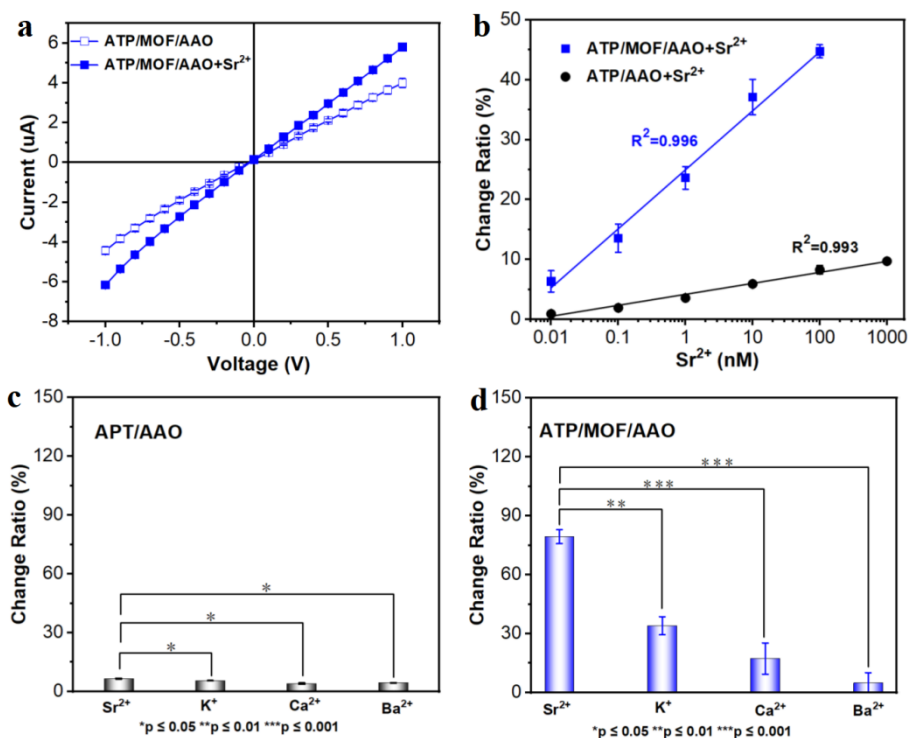


Figure 4. Sensitivity and specificity of ATP/AAO and APT/MOF/AAO detection for Sr²⁺. (a) I-V curves before and after APT/MOF/AAO response to 100 nM Sr²⁺. After exposure to Sr²⁺, APT/MOF/AAO exhibited an increase in ionic current. (b) The relationships between the increase in ionic current and the logarithm of Sr²⁺ concentration (0.01, 0.1, 1, 10, 100, and 1000 nM) for APT/AAO and APT/MOF/AAO, respectively. (c, d) Specificity of nanochannels with APT/AAO and APT/MOF/AAO for Sr²⁺ as well as three analogues, including K⁺, Ca²⁺, and Ba²⁺. APT/MOF/AAO demonstrates greatly improve detection sensitivity and specificity of Sr²⁺.

To compare the difference in sensitivity to differential pressure between the APT/AAO and APT/MOF/AAO, the relationships between ion current amplification and Sr²⁺ concentration were analyzed. As shown in **Figure 4b**, as the concentration of Sr²⁺ increased from 0.01 nM to 1000 nM, the transmembrane ion currents of

both the ATP/AAO and ATP/MOF/AAO exhibited gradual increases. For APT/AAO, the increase in ion current increased from 0.55% to 10%, with increases below 10% deemed invalid. Whereas, in APT/MOF/AAO, it escalated from 6.37% to 44.74%. Notably, the ion current increase in APT/MOF/AAO demonstrated a linear correlation with the logarithm of Sr^{2+} concentration. Upon reaching a 10% increase in transmembrane ion current, the Sr^{2+} ion concentrations detected by APT/AAO and APT/MOF/AAO were calculated to be 1000 nM and 0.03 nM, indicating the LOD of APT/AAO and APT/MOF/AAO reached 1000 nM and 0.03 nM, respectively. Remarkably, the LOD of Sr^{2+} detected by APT/MOF/AAO was approximately 3.3×10^4 times higher than that of APT/AAO.

To verify the specificity of nanochannels detection of Sr^{2+} , three other solutions containing similar metal ions K^+ , Ca^{2+} , and Ba^{2+} were chosen. Both APT/AAO and APT/MOF/AAO were immersed in 100 nM solutions of each metal ion, and the resulting ion current increases were recorded. As shown in **Figure 4c**, for APT/AAO, there was no significant difference in the ion current increase observed for the APT/AAO following immersion in the aforementioned four ion solutions. The significance analysis revealed a p-value ranging between 0.01 and 0.05, indicating only marginal statistical significance.

However, for APT/MOF/AAO, the ion current

increase following immersion in the Sr^{2+} solution was significantly higher compared to the other three ion solutions (**Figure 4d**). The respective current increases were 79.4%, 34.0%, 17.3%, and 4.9% for Sr^{2+} , K^+ , Ca^{2+} , and Ba^{2+} . The difference analysis yielded a p-value of less than or equal to 0.01. These findings highlight the remarkable sensing specificity of the APT/MOF/AAO, which exhibited superior specific recognition ability compared to the APT/AAO.

To evaluate the reliability of the APT/MOF/AAO sensing system in real water samples, we added 0, 1, and 10 nM Sr^{2+} to mineral water, tap water and seawater, respectively, to assess the recovery rate of Sr^{2+} in these three types of water samples. Subsequently, the resulting increase in ion current was recorded. The recovery rate and coefficient of variation (CV) were 94.00% to 118.70% and 2.89% to 9.35%, respectively (**Table 1**). These results indicate that the APT/MOF/AAO system exhibits high recovery rates and low variability in real water samples, highlighting its strong detection capabilities in such environments. We also discussed the impact of the sensor system's performance when it is in a high-salt ion solution (**Figure S3**). The result indicates that the APT/MOF/AAO sensor system can maintain stable detection performance in high salt ion solutions. Therefore, this sensing method can be applied in real seawater detection.

Table 1. Recovery of Sr^{2+} in real water samples based on APT/MOF/AAO.

Samples	Added (nM)	Tested (nM)	Recovery (%)	CV (%)
Mineral water	0	0.09	-----	-----
	1	1.03	94.00	4.42
	10	11.96	118.70	9.35
Tap water	0	0.05	-----	-----
	1	1.00	95.44	5.62
	10	10.63	105.88	4.43
seawater	0	0.02	-----	-----
	1	1.00	98.28	7.05
	10	11.41	113.88	2.89

3.4 Mechanism of enhanced sensing performance of APT/MOF/AAO.

To explore the enhanced sensitivity and specificity of Sr^{2+} detection by APT/MOF/AAO, a classical ionic conductance model was employed. When a voltage is applied, ions in the electrolytic solution are driven by an electric field to pass through the nanochannels, generating a current signal. This sensing system adheres to the universal ion conductivity model based on cylindrical nanochannels, where the ion current (I) in the nanochannels can be expressed by the following formula:^[41]

$$I = V \left[n_+ \mu_+ + n_- \mu_- \right] e \left(\frac{4h}{\pi D^2} + \frac{1}{D} \right)^{-1} + \frac{V \mu_{\oplus} \pi D \sigma}{h} \quad (1)$$

Where V represents trans-membrane voltage, h and D represent the thickness and pore size of the nanochannels, which regarded as an effective diameter; n_+ , n_- and μ_+ , μ_- represent the density and electrophoretic mobility of positive and negative ions,

respectively; e is the elementary charge; $(V \mu_{\oplus} \pi D \sigma) / h$ represents the ionic current through the highly surface-charged nanochannels. μ_{\oplus} here represents the mobility of ions in solution that are opposite to the charged pore charge, and the surface charge density is σ , which is the opposite sign of the opposite ionic charge. Our previous studies have demonstrated that when all electrolyte solutions in the experiment are concentrated at 0.1 M and the nanochannels pore size (D) is much smaller than its thickness, equation (1) can be simplified to the following equation:^[23]

$$I = V \left(\frac{4h}{\pi D^2} \right)^{-1} \quad (2)$$

From equation (2), it can be seen that effective pore size (D) of the nanochannels significantly influences the trans-membrane ion current in the experiment. Thus, we investigated the relationships between trans-membrane ion current and the effective pore size of APT/AAO and APT/MOF/AAO during detection (Figure 5).

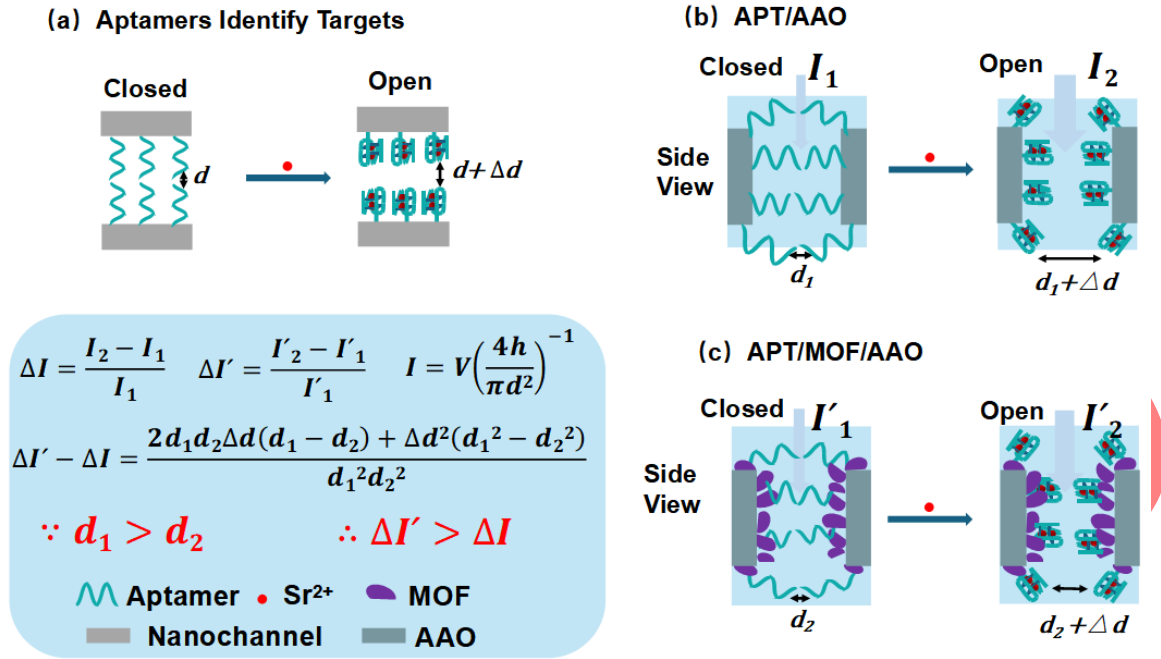


Figure 5. Schematic diagram of the sensing mechanisms of APT/AAO and APT/MOF/AAO. (a) Diagram of the process of aptamer-modified nanochannel recognition of Sr^{2+} . Before the target is recognized, the aptamer is stretched to clog the nanochannels (Closed), after binding to the target, the aptamer is induced by Sr^{2+} , and the aptamer folds into a G-quadruplex structure to open the nanochannel (Open). As a result, the nanopore diameter changes from d to $d+\Delta d$. (b, c) Side views of the APT/AAO and APT/MOF/AAO detection process, respectively. The results above indicate that the APT/MOF/AAO has higher sensitivity than APT/AAO due to the synergistic effect of 2D nanosheets and specific probes.

Before binding to the target, the aptamer within the nanochannels remains in a stretched configuration, causing a hindrance in the nanochannel current. However, owing to the strong binding affinity between Sr^{2+} and G-quadruplex, the aptamer transitions from its stretched state to a more stable G-quadruplex conformation upon Sr^{2+} induction. Consequently, the effective diameter of the nanochannels shifts from d to $d+\Delta d$ (Figure 5a). Here, we make the assumption that the effective pore size increment before and after binding to the target in both AAO and MOF is the same, denoted as Δd . Upon binding to the target, the effective pore size of the APT/AAO increases from d_1 to $d_1+\Delta d$, while that of the APT/MOF/AAO nanochannels increases from d_2 to $d_2+\Delta d$ (Figure 5b and 5c). In the experiment, the increase in ion currents for the APT/AAO and APT/MOF/AAO can be represented as ΔI and $\Delta I'$, respectively, as follows:

$$\Delta I = \frac{I_2 - I_1}{I_1} \quad (3)$$

$$\Delta I' = \frac{I'_2 - I'_1}{I'_1} \quad (4)$$

Where the I_1 and I_2 represent the ion currents before and after the APT/AAO binds to the target, and I'_2 and I'_1 represent the ion currents before and after the APT/MOF/AAO binds to the target. To compare the increase in ion currents between the APT/AAO and APT/MOF/AAO after binding to the target, we calculated the difference between $\Delta I'$ and ΔI as follows:

$$\Delta I' - \Delta I = \frac{2d_1d_2\Delta d(d_1 - d_2) + \Delta d^2(d_1^2 - d_2^2)}{d_1^2d_2^2} \quad (5)$$

Through previous SEM and AFM images of APT/MOF/AAO, it was confirmed that the nanochannels were filled and covered with dense layers of 2D nanosheets on the inner walls and outer surfaces of AAO. This feature causes the effective pore size of the APT/MOF/AAO to be much narrower, resulting in a smaller effective pore size than that of the APT/AAO ($d_2 < d_1$). Based on this observation and Eq. (5), when $\Delta I' - \Delta I > 0$ is calculated, it becomes evident that the ion current increase of the APT/MOF/AAO

surpasses that of the APT/AAO upon binding with Sr^{2+} . These findings suggest that the enhanced sensitivity and specificity of Sr^{2+} detection with APT/MOF/AAO can be attributed to the reduction of the effective mass transfer pathway within the nanochannels by the 2D nanosheets, along with the synergistic effect of aptamers with the stable structure formed by the target.

3.5 Experiment were modeled using COMSOL.

To further corroborate our findings, we conducted simulations using COMSOL Multiphysics 6.0. COMSOL modeling diagram of the potential distribution of nanochannels is illustrated in **Figure 6a**. This model comprises two cells identical to the top and bottom, with nanochannels situated in the middle. For more detailed parameters of the model, please refer to **Figure S5** and **Table S2**. The potential within the nanochannels channel gradually diminishes from top to bottom. The nanochannels have diameters of 75, 60,

26, and 10 nm, respectively, with an initial electrolyte concentration of 10 mol/m³. Given the focus on the synergistic effect from decreased nanochannel's effective diameter by MOF and specific binding of Sr^{2+} by aptamer, the influence of nanochannel surface charge is disregarded in this context. Based on the constructed COMSOL model, the outcomes were displayed in **Figure 6b** and **6c**. After Sr^{2+} is recognized by APT/AAO and APT/MOF/AAO, the ion current was larger than that before recognition. Furthermore, the ionic current change ratio before and after the recognition of Sr^{2+} by APT/MOF/AAO nanochannels exceeds that of APT/AAO (**Figure 6d**). The ion current change ratio of APT/MOF/AAO was calculated to be 452%, approximately 8.3 times higher than APT/AAO's 54.5%. This indicates that APT/MOF/AAO is more sensitive than APT/AAO in detecting Sr^{2+} . In conclusion, the calculations' results align closely with the experimental results.

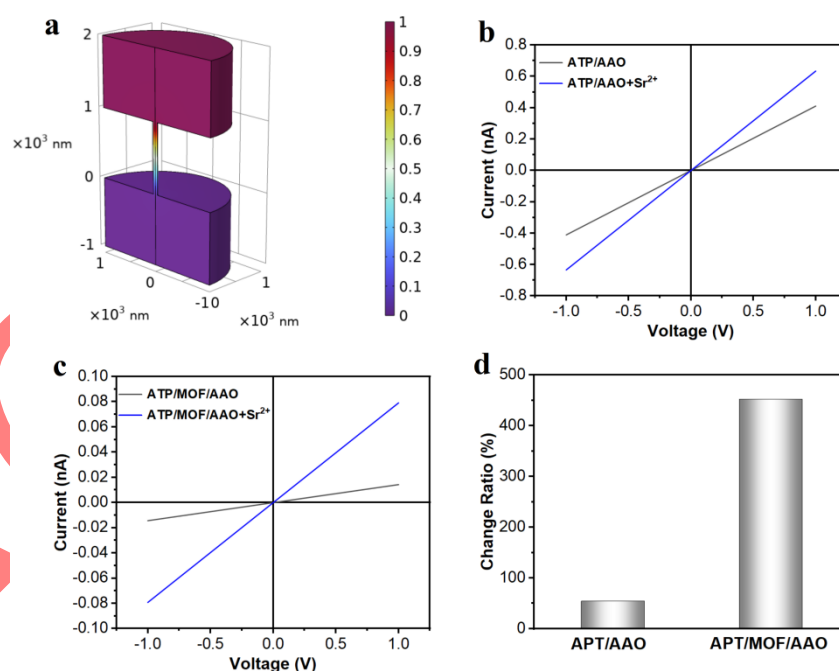


Figure 6. Simulation of ionic current in APT/AAO and APT/MOF/AAO. (a) COMSOL modeling diagram of the potential distribution of nanochannels during testing. (b, c) I-V curves before and after binding to the target for APT/AAO and APT/MOF/AAO, respectively. The current increases after APT/AAO and APT/MOF/AAO bind to the targets. (d) Amplification of ion current ratio after target recognition by APT/AAO and APT/MOF/AAO. The increase in ion current after recognition of the target by APT/MOF/AAO is much larger than that of APT/AAO.

Conclusions

Due to the numerous advantages of the biochemical sensing system in nanochannels, such as speed, high

sensitivity, specificity, label-free operation, and excellent throughput, solid-state nanochannels modified with 2D nanomaterials and specific aptamers were designed for the high-sensitivity detection of Sr^{2+} . In the process of Sr^{2+} recognition, the synergistic effect from decreased nanochannel's effective diameter by MOF and specific binding of Sr^{2+} by aptamer, thereby significantly amplifying the difference in ionic current signals. As a result, the LOD of APT/MOF/AAO has been reduced from 1000 nM to 0.03 nM compared to the APT/AAO. Furthermore, the sensing mechanism of nanochannels was elucidated using the general ion conductivity model of cylindrical nanochannels, while COMSOL simulations corroborated the increase in ion currents in the nanochannels before and after binding to the target, aligning closely with experimental findings. Additionally, APT/MOF/AAO also demonstrated robust capability in reliably detecting nanomolar levels of Sr^{2+} in complex samples. This research enhances understanding of the synergistic effects of nanochannels and offer significant insights into developing solid-state nanochannels with higher sensitivity for analyzing samples from complex environments.

Acknowledgements

National Natural Science Foundation of China (22090050, 22090052, 22176180), National Basic Research Program of China (2021YFA1200400), the Natural Science Foundation of Hubei Province (2024AFA001), Shenzhen Science and Technology Program (No.JCYJ20220530162406014).

Reference

[1] Kaidarova A, Geraldi N R, Wilson R P, Kosel J, Meekan M G, Eguiluz V M, Hussain M M, Shamim A, Liao H and Srivastava M. Wearable sensors for monitoring marine environments and their inhabitants[J]. *Nature Biotechnology*, 2023, 41(9): 1208-1220.

[2] da Costa Filho B M, Duarte A C and Rocha-Santos T A P. Environmental monitoring approaches for the detection of organic contaminants in marine

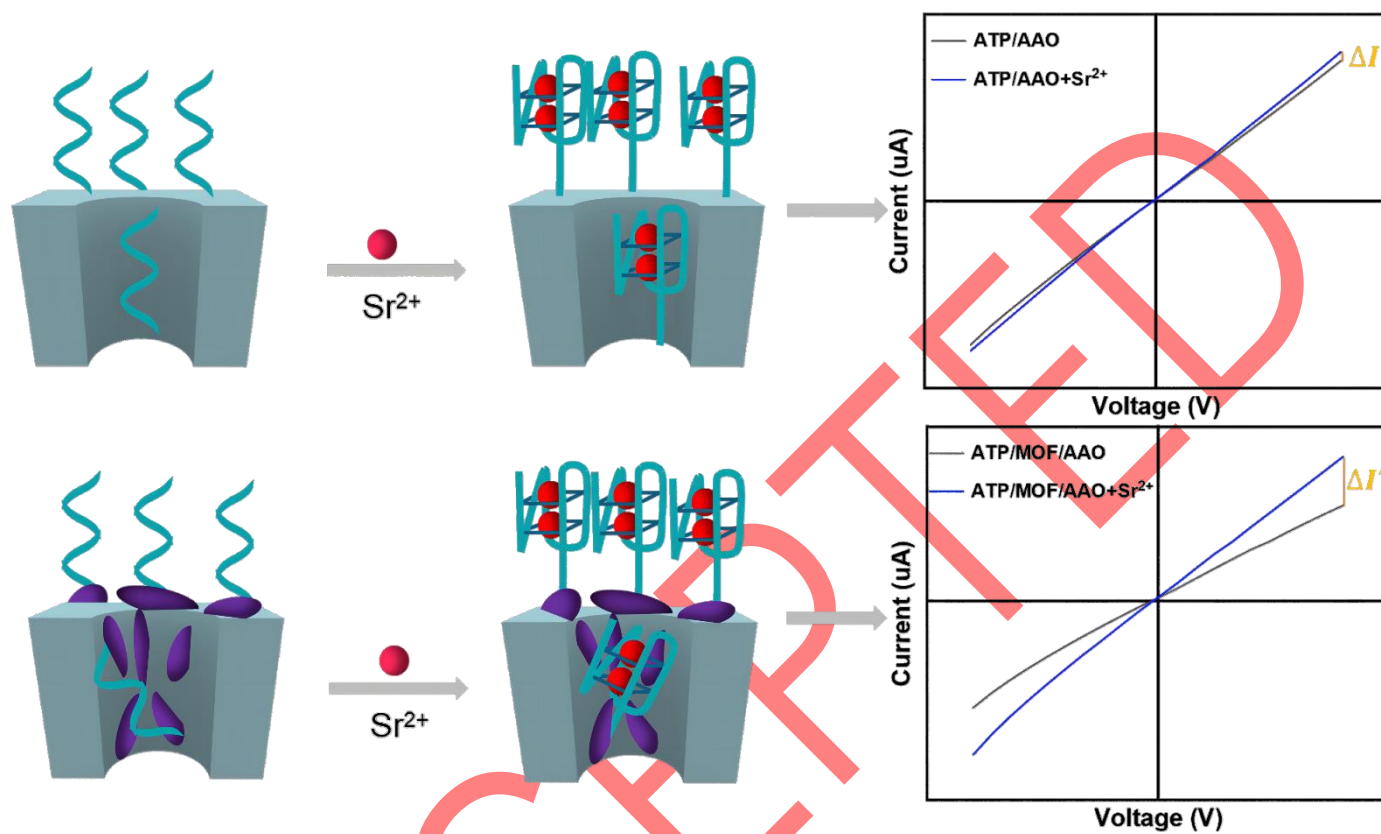
environments: A critical review[J]. *Trends in Environmental Analytical Chemistry*, 2022, 33.

- [3] Alam I, Rehman J u, Ahmad N, Nazir A, Hameed A and Hussain A. An overview on the concentration of radioactive elements and physiochemical analysis of soil and water in Iraq[J]. *Reviews on environmental health*, 2020, 35(2): 147-155.
- [4] Bolobajev J, Leier M, Vaasma T, Nilb N and Salupere S. Laboratory and pilot plant scale study on the removal of radium, manganese and iron from drinking water using hydrous manganese oxide slurry[J]. *Journal of Environmental Chemical Engineering*, 2022, 10(6): 108942.
- [5] Farouk M I H Z, Jamil Z and Latip M F A. Towards online surface water quality monitoring technology: A review[J]. *Environmental Research*, 2023: 117147.
- [6] Agberien A V and Örmeci B. Monitoring of cyanobacteria in water using spectrophotometry and first derivative of absorbance[J]. *Water*, 2019, 12(1): 124.
- [7] Xu Z, Zhou W, Dong Q, Li Y, Cai D, Lei Y, Bagtzoglou A and Li B. Flat flexible thin millielectrode array for real-time in situ water quality monitoring in distribution systems[J]. *Environmental Science: Water Research & Technology*, 2017, 3(5): 865-874.
- [8] Uppuluri K, Szwagierczak D, Fernandes L, Zaraska K, Lange I, Synkiewicz-Musialska B and Manjakkal L. A high-performance pH-sensitive electrode integrated with a multi-sensing probe for online water quality monitoring[J]. *Journal of Materials Chemistry C*, 2023, 11(44): 15512-15520.
- [9] Lu Y, Li P, Yan H and Shen S. Ionic liquid modified porous polymer as a dispersive filter extraction adsorbent for simple, sensitive, and efficient determination of chlorotriazine herbicides in irrigation water[J]. *Journal of Agricultural and Food Chemistry*, 2022, 70(4): 1327-1334.
- [10] Izquierdo J E E, Cavallari M R, García D C, Oliveira J D d S, Nogueira V A M, Braga G d S, Ando Junior O H, Quivy A A, Kymissis I and Fonseca F J. Detection of water contaminants by organic transistors as gas sensors in a bottom-

- gate/bottom-contact cross-linked structure[J]. 46
Sensors, 2023, 23(18): 7981. 47
- [11] Novaes C G, Bezerra M A, da Silva E G P, dos 48
Santos A M P, da Silva Romao I L and Neto J H S. 49
A review of multivariate designs applied to the 50
optimization of methods based on inductively 51
coupled plasma optical emission spectrometry 52
(icp oes)[J]. Microchemical journal, 2016, 128: 53
331-346. 54
- [12] Li Q, Ying Y-L, Liu S-C, Lin Y and Long Y-T. 55
Detection of single proteins with a general 56
nanopore sensor[J]. ACS sensors, 2019, 4(5): 57
1185-1189. 58
- [13] Ying Y L, Gao R, Hu Y X and Long Y T. 59
Electrochemical confinement effects for 60
innovating new nanopore sensing mechanisms[J]. 61
Small Methods, 2018, 2(6): 1700390. 62
- [14] Long Y and Zhang M. Self-assembling bacterial 63
pores as components of nanobiosensors for the 64
detection of single peptide molecules[J]. Science 65
in China Series B: Chemistry, 2009, 52(6): 731-66
733. 67
- [15] Yang H and Qing G. Solid-state nanopores and 68
nanochannels for the detection of biomolecules[J]. 69
Chemical Physics Reviews, 2021, 2(2). 70
- [16] Liu L, Yang C, Zhao K, Li J and Wu H-C. Ultrashort 71
single-walled carbon nanotubes in a lipid bilayer 72
as a new nanopore sensor[J]. Nature 73
communications, 2013, 4(1): 2989. 74
- [17] Hou X, Zhang H and Jiang L. Building bio-inspired 75
artificial functional nanochannels: From symmetric 76
to asymmetric modification[J]. Angewandte 77
Chemie International Edition, 2012, 51(22): 5296-78
5307. 79
- [18] Deng J, Liu C and Sun J. DNA - based 80
nanomaterials for analysis of extracellular 81
vesicles[J]. Advanced Materials, 2023: 2303092. 82
- [19] Bodily T A, Ramanathan A, Wei S, Karkisaval A, 83
Bhatt N, Jerez C, Haque M A, Ramil A, Heda P 84
and Wang Y. In pursuit of degenerative brain 85
disease diagnosis: Dementia biomarkers detected 86
by DNA aptamer-attached portable graphene 87
biosensor[J]. Proceedings of the National 88
Academy of Sciences, 2023, 120(47): 89
e2311565120. 90
- [20] Ban D K, Liu Y, Wang Z, Ramachandran S, Sarkar 91
N, Shi Z, Liu W, Karkisaval A G, Martinez-Loran E 92
and Zhang F. Direct DNA methylation profiling with 93
an electric biosensor[J]. ACS nano, 2020, 14(6): 94
6743-6751. 95
- [21] Wang J, Hou J, Zhang H, Tian Y and Jiang L. 96
Single nanochannel-aptamer-based biosensor for 97
ultrasensitive and selective cocaine detection[J]. 98
ACS applied materials & interfaces, 2018, 10(2): 99
2033-2039. 100
- [22] Ma Q, Chu W, Nong X, Zhao J, Liu H, Du Q, Sun 101
J, Shen J, Lu S-M and Lin M. Local electric 102
potential-driven nanofluidic ion transport for 103
ultrasensitive biochemical sensing[J]. ACS nano, 104
2024. 105
- [23] Liu L, Luo C, Zhang J, He X, Shen Y, Yan B, Huang 106
Y, Xia F and Jiang L. Synergistic effect of bio- 107
inspired nanochannels: Hydrophilic DNA probes 108
at inner wall and hydrophobic coating at outer 109
surface for highly sensitive detection[J]. Small, 110
2022, 18(37): 2201925. 111
- [24] Meng D, Hao C, Cai J, Ma W, Chen C, Xu C, Xu L 112
and Kuang H. Tailored chiral copper selenide 113
nanochannels for ultrasensitive enantioselective 114
recognition and detection[J]. Angewandte Chemie, 115
2021, 133(47): 25201-25208. 116
- [25] Zeng H, Zhou S, Xie L, Liang Q, Zhang X, Yan M, 117
Huang Y, Liu T, Chen P and Zhang L. Super- 118
assembled mesoporous thin films with 119
asymmetric nanofluidic channels for sensitive and 120
reversible electrical sensing[J]. Biosensors and 121
Bioelectronics, 2023, 222: 114985. 122
- [26] Qiao Y, Hu J J, Hu Y, Duan C, Jiang W, Ma Q, 123
Hong Y, Huang W H, Xia F and Lou X. Detection 124
of unfolded cellular proteins using nanochannel 125
arrays with probe-functionalized outer surfaces[J]. 126
Angewandte Chemie International Edition, 2023, 127
62(43). 128
- [27] Han B and Chakraborty A. Highly efficient 129
adsorption desalination employing protonated- 130
amino-functionalized mofs[J]. Desalination, 2022, 131
541: 116045. 132
- [28] Cheng P, Liu Y, Wang X, Fan K, Li P and Xia S. 133
Regulating interfacial polymerization via 134
constructed 2d metal-organic framework 135

- interlayers for fabricating nanofiltration membranes with enhanced performance[J]. Desalination, 2022, 544.
- [29] Ying Y, Zhang Z, Peh S B, Karmakar A, Cheng Y, Zhang J, Xi L, Boothroyd C, Lam Y M and Zhong C. Pressure-responsive two-dimensional metal-organic framework composite membranes for CO₂ separation[J]. *Angewandte Chemie International Edition*, 2021, 60(20): 11318-11325.
- [30] Doustkhah E, Hassandoost R, Khataee A, Luque R and Assadi M H N. Hard-templated metal-organic frameworks for advanced applications[J]. *Chemical Society Reviews*, 2021, 50(5): 2927-2953.
- [31] Qiu M, Zhu Z, Wang D, Xu Z, Miao W, Jiang L and Tian Y. Large-scale metal-organic framework nanoparticle monolayers with controlled orientation for selective transport of rare-earth elements[J]. *Journal of the American Chemical Society*, 2023, 145(22): 12275-12283.
- [32] Ingram B and Sloan D. Strontium isotopic composition of estuarine sediments as paleosalinity-paleoclimate indicator[J]. *Science*, 1992, 255(5040): 68-72.
- [33] Jiang Y, Ma W, Qiao Y, Xue Y, Lu J, Gao J, Liu N, Wu F, Yu P and Jiang L. Metal-organic framework membrane nanopores as biomimetic photoresponsive ion channels and photodriven ion pumps[J]. *Angewandte Chemie International Edition*, 2020, 59(31): 12795-12799.
- [34] Huang H, Suslov N B, Li N-S, Shelke S A, Evans M E, Koldobskaya Y, Rice P A and Piccirilli J A. A g-quadruplex - containing rna activates fluorescence in a gfp-like fluorophore[J]. *Nature Chemical Biology*, 2014, 10(8): 686-691.
- [35] Pu F, Wu L, Ran X, Ren J and Qu X. G-quartet-based nanostructure for mimicking light - harvesting antenna[J]. *Angewandte Chemie International Edition*, 2015, 54(3): 892-896.
- [36] Biffi G, Tannahill D, McCafferty J and Balasubramanian S. Quantitative visualization of DNA g-quadruplex structures in human cells[J]. *Nature Chemistry*, 2013, 5(3): 182-186.
- [37] Yang C, Liu L, Zeng T, Yang D, Yao Z, Zhao Y and Wu H-C. Highly sensitive simultaneous detection of lead(ii) and barium(ii) with g-quadruplex DNA in α -hemolysin nanopore[J]. *Analytical Chemistry*, 2013, 85(15): 7302-7307.
- [38] Trajkovski M, Webba da Silva M and Plavec J. Unique structural features of interconverting monomeric and dimeric g-quadruplexes adopted by a sequence from the intron of the n-myc gene[J]. *Journal of the American Chemical Society*, 2012, 134(9): 4132-4141.
- [39] Akhshi P, Mosey N J and Wu G. Free-energy landscapes of ion movement through a g-quadruplex DNA channel[J]. *Angewandte Chemie*, 2012, 124(12): 2904-2908.
- [40] Kankia B I and Marky L A. Folding of the thrombin aptamer into a g-quadruplex with sr²⁺: Stability, heat, and hydration[J]. *Journal of the American Chemical Society*, 2001, 123(44): 10799-10804.
- [41] Wanunu M. Nanopores: A journey towards DNA sequencing[J]. *Physics of life reviews*, 2012, 9(2): 125-158.

TOC

1
2
3
4
5
6
7
8
9
10
11
12
13
14
15
16
17
18
19
20

金属有机框架功能化的纳米通道对锶离子进行高灵敏度检测

王旭刚^a, 何正旭^a, 丁德芳^a, 罗雪芹^a, 戴力^a, 张炜奇^a, 马群^b, 黄羽^{a*}, 夏帆^{a,c}

(a. 中国地质大学材料科学与化学学院, 纳米地质材料教育部工程研究中心, 生物地质与环境地质国家重点实验室, 武汉 430074; b. 大阪都立大学研究生院工学研究科化学工程系, 日本 大阪堺市 599-8570; c. 中国地质大学深圳研究院)

摘要: 锶-90 是一种高放射性同位素, 在食物链和骨骼结构中积累, 对人类健康构成重大风险。在复杂的环境水样中, 迫切需要一种高灵敏的锶-90 检测策略。在这里, 金属有机框架 (Metal Organic Frameworks) 和特异性适配体修饰的固态纳米通道被设计用于高灵敏度的 Sr^{2+} 检测。MOF 导致的纳米通道有效孔径减小与适配体对 Sr^{2+} 的特异性结合之间的协同作用放大了离子电流信号的差异, 显著提高了检测灵敏度。MOF 修饰的纳米通道对 Sr^{2+} 表现出高灵敏度的检测, 检测限 (LOD) 低至 0.03 nM, 然而没有修饰 MOF 纳米片的 AAO 的 LOD 仅为 1000 nM。结果表明, MOF 修饰的纳米通道对 Sr^{2+} 的检测限 LOD 比未修饰 MOF 的纳米通道高约 33,000 倍。仿真模拟计算结果与这一实验趋势完全吻合。此外, 加标回收实验还实现了对各种水样中 Sr^{2+} 的高度可靠性检测, 回收率在 94.00% 至 118.70% 之间, 变异系数低至 2.89% 至 9.35% 之间。APT/MOF/AAO 传感系统在真实水样中表现出高回收率和低变异性, 凸显了其在此类环境中的强大检测能力。这项研究为快速发展的先进纳米通道传感器领域及其在分析复杂样品方面的各种应用提供了宝贵的见解, 包括环境污染物检测、食品分析、医疗诊断等。

关键词: 纳米通道; 金属有机框架; 传感器; 锶离子; 高灵敏检测